



**HAL**  
open science

# An Image Rendering Pipeline for Focused Plenoptic Cameras

Matthieu Hog, Neus Sabater, Benoît Vandame, Valter Drazic

► **To cite this version:**

Matthieu Hog, Neus Sabater, Benoît Vandame, Valter Drazic. An Image Rendering Pipeline for Focused Plenoptic Cameras. 2017. hal-01401501v2

**HAL Id: hal-01401501**

**<https://hal.science/hal-01401501v2>**

Preprint submitted on 14 Jun 2017

**HAL** is a multi-disciplinary open access archive for the deposit and dissemination of scientific research documents, whether they are published or not. The documents may come from teaching and research institutions in France or abroad, or from public or private research centers.

L'archive ouverte pluridisciplinaire **HAL**, est destinée au dépôt et à la diffusion de documents scientifiques de niveau recherche, publiés ou non, émanant des établissements d'enseignement et de recherche français ou étrangers, des laboratoires publics ou privés.

# An Image Rendering Pipeline for Focused Plenoptic Cameras

Matthieu Hog, Neus Sabater, Benoît Vandame, Valter Drazic  
Technicolor Research & Innovation

**Abstract**—In this paper, we present a complete processing pipeline for focused plenoptic cameras. In particular, we propose (i) a new algorithm for microlens center calibration fully in the Fourier domain, (ii) a novel algorithm for depth map computation using a *stereo focal stack* and (iii) a depth-based rendering algorithm that is able to refocus at a particular depth or to create all-in-focus images. The proposed algorithms are fast, accurate and do not need to generate subaperture images or epipolar plane images which is capital for focused plenoptic cameras. Also, the resolution of the resulting depth map is the same as the rendered image. We show results of our pipeline on the Georgiev’s dataset and real images captured with different Raytrix cameras.

**Index Terms**—Plenoptic cameras, calibration, depth estimation, refocusing

## I. INTRODUCTION

**L**IGHT FIELDS (LF) offer new applications compared to conventional images. For example, it is possible to modify the virtual focus plane after the shot (digital refocusing [1], [2]) or to render images with a greater depth of field compared to the main lens optics capabilities [3]. Besides, a LF contains both angular and spatial information of the incoming light rays, allowing to estimate the depth of the captured scene, which is one major benefit of the LF technology.

Plenoptic cameras have become popular because they are able to capture a LF thanks to a microlens array (MLA) placed between the main lens and the sensor. Depending on the MLA position, plenoptic cameras are divided into type 1 [1] such as the Lytro cameras [4], and type 2 or *focused* [5] such as the Raytrix cameras [6]. Fig. 1 illustrates the two camera designs. In the type 1, the main lens is focused on the microlenses and the microlenses are focused at infinity. With this design, each pixel images only one part of the main lens corresponding to one light ray direction. In the type 2, the MLA is placed such that  $\frac{1}{a} + \frac{1}{b} = \frac{1}{f}$ , so each pixel images an area of the entrance pupil, integrating light rays with different directions. Also, type 2 cameras have a better spatial resolution but less angular resolution compared to type 1 cameras. Depending on the application, one type of camera or the other would be more advantageous.

Another difference due to the distinct plenoptic designs concerns the Subaperture Images (SAIs) and Epipolar Plane Images (EPIs) computation. Considering the two plane parametrization to represent a 4D Light Field  $L(x, y, u, v)$  as in [7] [8], SAIs and EPIs are nothing else than slices of  $L(x, y, u, v)$ . Each SAI is an image of the same scene for a fixed viewing angle  $(u, v)$  and each EPI is an image obtained fixing  $(y, v)$ . By construction, SAIs are easily generated for type 1 plenoptic cameras but not for type 2. Indeed, for

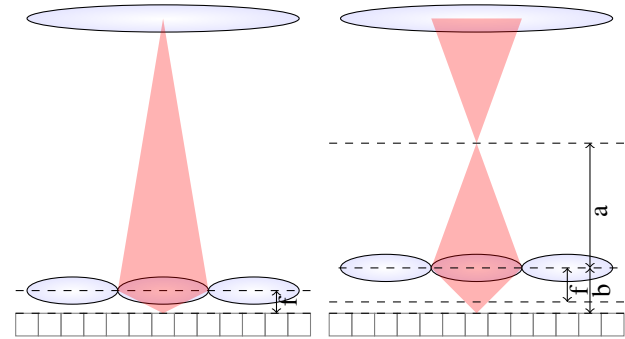


Fig. 1: Plenoptic camera designs: type 1 (left) and type 2 or focused (right).

type 1 cameras, each SAI is created taking all pixels at the same relative position in the microlens with respect to the microlens center [1]. On the contrary, generating SAIs without strong artifacts on type 2 cameras requires to first estimate the depth [9], [10]. Besides, generating SAIs also causes aliasing artifacts, as pointed out by [11].

In this paper, we propose a complete pipeline for focused plenoptic cameras including microlens calibration, depth estimation and rendering. First, we have designed a calibration algorithm, entirely in the Fourier domain, that has proved to be fast, insensitive to noise and robust to different MLA configurations (different microlens radius, offset, rotation etc.). Furthermore, even if it is not the scope of the paper, we also give some hints on how our calibration could be used on natural images and more complex MLA geometries.

While our calibration is independent of the type of plenoptic camera, the method we propose for depth estimation is specialized for type 2 cameras. Indeed, the main asset of our approach is that SAIs or EPIs are not computed. Instead, the data captured in the sensor plane is directly projected into the rendering plane, in which depth estimation is performed.

Finally, we show how the generated depth maps in the image domain can be used during the rendering step. In particular, we show how to render all-in-focus images and how to correct angular aliasing.

To sum up, our contributions are (see Fig. 2):

- 1) A calibration algorithm in the Fourier domain for fast and accurate microlens images center estimation.
- 2) A novel depth estimation algorithm operating in the refocused image domain that exploits the relationship between the focus planes and the disparities on each slice of what we define as a *stereo focal stack*.
- 3) A depth-based rendering algorithm that is able to pro-

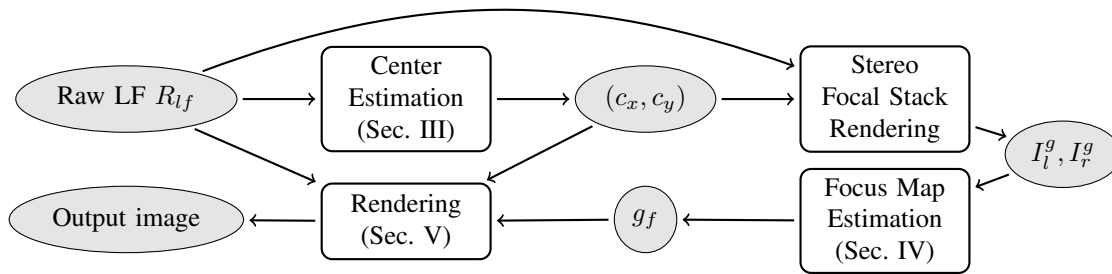


Fig. 2: Proposed pipeline to process a raw LF captured with a focused plenoptic camera. Microlens centers are first estimated. Then a *stereo focal stack* is computed projecting directly the data from the sensor. The *stereo focal stack* allows to estimate a focus map, which is used in the final rendering step.

duce accurate results for image refocusing and all-in-focus imaging.

## II. RELATED WORK

Regarding plenoptic camera calibration several solutions have already been explored either in the spatial domain [12], or using a combination of Fourier and spatial analysis [13], [14]. However our algorithm estimates all parameters on the frequency domain which has the advantage of being fast and accurate.

In the literature, plenoptic depth estimation has aroused great interest and many research works have been published. We classify them in four different approaches depending on the image type they consider as input: SAIs, microlens images, EPIs or refocused images.

First, SAI-based depth estimation methods rely on the fact that computed SAIs from plenoptic cameras are well rectified images with constant baseline. Among these techniques, we can find local block-matching [15]–[17] and global matching methods [18]–[20]. Then, microlens-based depth estimation methods consider each microlens image as separated camera images with a very small baseline. For this type of methods local and global approaches are also adapted to the plenoptic framework. In [21]–[23] a block-matching algorithm for microlens images is used, and [24]–[26] formalize the problem as an energy minimization task in which cost volumes are computed for each microlens.

Another type of method for plenoptic depth-estimation uses EPIs [27]–[31]. Indeed, the slope of the line composed of corresponding pixel in an EPI is proportional to the depth of the pixel [32].

Finally, other approaches use refocused images or images in a focal stack to perform depth computation [33], [34]. However, when defocus cues are used they are usually combined with other measures [18], [29] because of their poor accuracy.

Among plenoptic depth estimation methods we would like to highlight some recent approaches that explicitly estimate occlusions and seem to give the best results. Occlusions can be detected by studying the variance of the pixel re-projections on several views as in [35] or an occlusion coefficient can be used in a regularisation framework. For instance, [36] statistically computes the probability of a pixel to be in an occlusion boundary, [37] uses the log likelihood of the probability of the

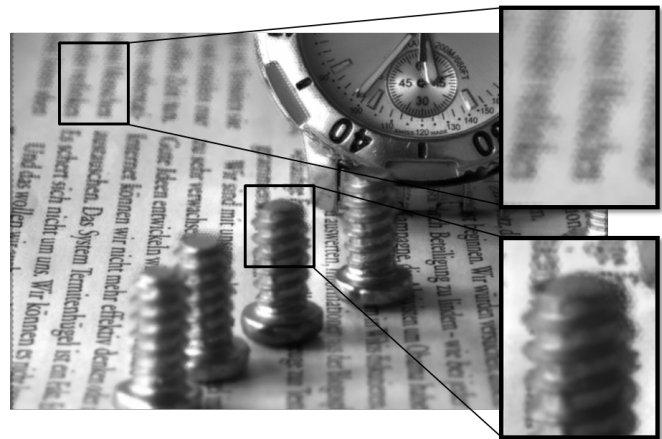


Fig. 3: SAI from a focused plenoptic camera estimated with the approach in [9]. Note the microlens artifacts on the two zoom-ins that may be detrimental to depth estimation (please see on the electronic version). Unlike type 1, rendering SAIs without errors in a type 2 plenoptic cameras requires to know the depth. Our approach circumvents this problem estimating depth without SAIs.

pixel color to appear in the projected views and [38] compares depth and variance of occluding candidates normalized by the region mean (to handle uniform areas). It is also possible to learn occlusion and depth simultaneously as in [39].

While plenty of contributions on plenoptic depth estimation significantly improving the state-of-the-art have been published the last years, few papers address the problem for the type 2 plenoptic setup. This may be due to the fact that most of the available data come from Lytro (type 1) cameras. Moreover, the proposed approaches almost all rely on re-sampling the captured LF to a traditional SAI-based representation. Yet, SAIs or EPIs are not well adapted to type 2 plenoptic cameras [21], [40]. Indeed, it has been proved [11] that SAIs suffer from strong aliasing artifacts (even with anti-aliasing filters) which affects depth estimation. But above all, as mentioned in the introduction, estimating SAIs or EPIs for type 2 plenoptic cameras is prone to errors. In [9], the authors point out that depth needs to be known for computing SAIs on type 2 cameras while depth estimation methods are based on

SAIs (chicken-egg problem). So, in [9] it is proposed to stitch hexagonal patches of different diameters to form the SAIs. Since depth is unknown, the diameter is computed such that the gradient at the patch borders is minimized. This processing is not without errors, especially in the out of focus areas and objects edges (see Fig. 3).

MicroLens-based methods [21] can be a good alternative for focused plenoptic cameras provided the size of the microlenses are big enough as it happens to be with the Georgiev’s prototype, but this is not always the case.

In this context, our motivation is to provide a depth estimation method that works with arbitrarily sized microlenses and operates in the refocusing image domain without the need of SAIs or EPIs. This approach has the advantage of creating depth maps of the resolution of the final rendered image and that are not affected by SAI rendering artifacts.

Concerning plenoptic image rendering, many algorithms have been proposed since the pioneer work of [1] using the Fourier Slice Theorem. On the one hand, there are approaches using SAIs (shift and add) [14], [41] and on the other hand, the approaches using the projection rendering algorithm [13], [42] which are the closer works to ours.

### III. PLENOPTIC IMAGE CALIBRATION

In this work, plenoptic calibration refers to estimating the microlens image centers (see [43] for a complete plenoptic camera calibration method). More precisely, in our calibration, we compute the microlens image diameter  $D$ , the translation offset  $\mathbf{o} = (o_x, o_y)$  and the rotation  $\alpha$  with respect to the coordinate system given by the sensor array (see Fig. 4).

So, the microlens image center coordinates  $(c_x, c_y)$  in the pixel coordinates are computed as:

$$\begin{bmatrix} c_x \\ c_y \end{bmatrix} = \begin{bmatrix} o_x \\ o_y \end{bmatrix} + \frac{D}{\sqrt{3}} \begin{bmatrix} 1 & 1/2 \\ 0 & \sqrt{3}/2 \end{bmatrix} \begin{bmatrix} \cos(\alpha) & -\sin(\alpha) \\ \sin(\alpha) & \cos(\alpha) \end{bmatrix} \begin{bmatrix} x \\ y \end{bmatrix}, \quad (1)$$

where  $(x, y) \in \mathbb{Z}^2$  are the elements of an integer grid.

Our approach leans on the observation that a white plenoptic image  $I_w$  can be modeled as a sum of three 2D cosines (see Fig. 5), oscillating at different angles:

$$I_w(x, y) = \frac{1}{3} \sum_{d=0}^2 \cos\left(\frac{2\pi}{D} c^d(x, y)\right), \quad (2)$$

$$c^d(x, y) = \cos\left(\frac{d\pi}{3} + \alpha\right)(x - o_x) + \sin\left(\frac{d\pi}{3} + \alpha\right)(y - o_y).$$

Consequently, its Fourier transform  $F(I_w)$  is a Dirac comb function. In this work we propose to estimate all calibration parameters  $\alpha$ ,  $D$  and  $\mathbf{o}$  directly from  $F(I_w)$ .

Let  $F^m$  and  $F^p$  be the magnitude and phase of  $F(I_w)$ . Let  $\xi_i^0 \in \mathbb{Z}^2$  be the pixel coordinates of the  $i$ -th peak (local maxima) of  $F^m$  obtained by thresholding. In practice our threshold is fixed to  $100 \cdot \text{Variance}(F^m)$ . Note however, that the peaks of the Dirac comb in the frequency domain need to be evaluated with great accuracy (much below the pixel size) in order to obtain precise microlens image centers. Inspired by [44], the final peak locations  $\xi_i = \xi_i^0 + \Delta\xi_i^0 \in \mathbb{R}^2$  are estimated with sub-pixel accuracy.

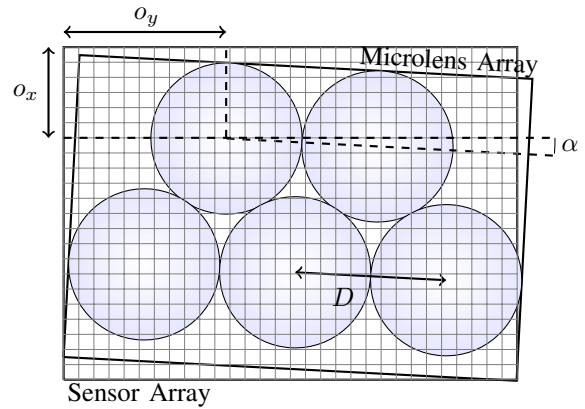


Fig. 4: Microlens images (of diameter  $D$ ) are arranged in a hexagonal grid and pixels in a squared grid. Microlens images are misaligned with respect to the pixel grid. There is a rotation of angle  $\alpha$  and a translation offset  $(o_x, o_y)$  between the origins of both grids placed at the most top-left pixel and microlens image respectively.

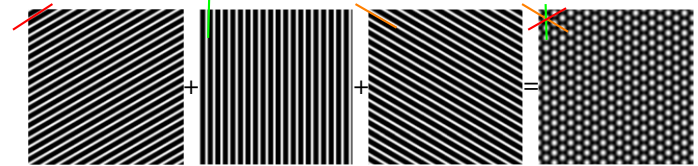


Fig. 5: An ideal white plenoptic image is a sum of three 2D cosine images. The intersection of the lines along which the 3 cosines oscillate defines the offset  $\mathbf{o}$  of the white image.

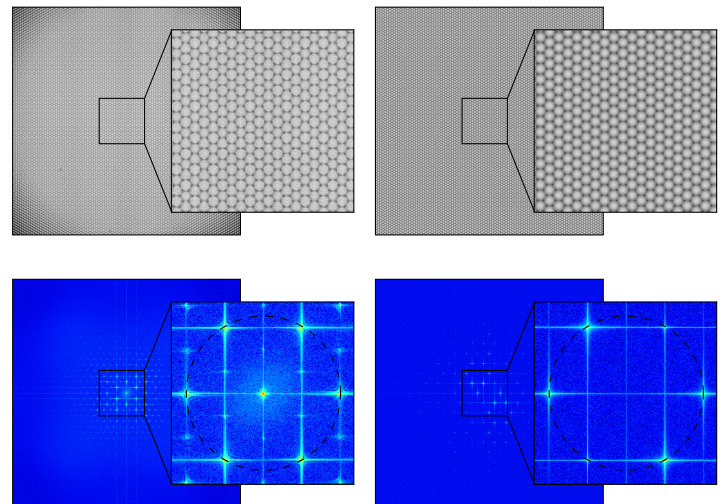


Fig. 6: Comparison of a white image synthesized with our model (right) versus a real white Raytrix image (left). The two images are visually similar (top) but the important similarity lies in the Fourier (log) frequency spectrum (bottom). The Fourier transform of an ideal white image is a perfect Dirac comb with 6 peaks at a constant frequency radius. On real white image many replicas appear. Our algorithm selects the six concentric peaks with highest energy.

More precisely, each component of  $\Delta\xi^0 = (\Delta\xi_u^0, \Delta\xi_v^0)$  is computed as

$$\text{sign}(F^m(\xi^-) - F^m(\xi^+)) \frac{M}{M + F^m(\xi^0)},$$

where  $M = \max\{F^m(\xi^+), F^m(\xi^-)\}$ , (3)

and  $\xi^+ = (\xi_u^0 + 1, \xi_v^0)$ ,  $\xi^- = (\xi_u^0 - 1, \xi_v^0)$  when estimating  $\Delta\xi_u^0$  and  $\xi^+ = (\xi_u^0, \xi_v^0 + 1)$ ,  $\xi^- = (\xi_u^0, \xi_v^0 - 1)$  when estimating  $\Delta\xi_v^0$ .

The number of peaks,  $\text{card}(i)$ , is equal to six in the ideal case of the white image being a sum of pure cosines (Eq. 2) but many replicas appear on real images. In that case, we select the six peak locations with most energy and at the same distance from the center (Fig 6).

The microlens images diameter and the rotation are then computed as

$$D = \frac{N}{\frac{1}{6} \sum_{i=1}^6 \rho_i}, \quad (4)$$

$$\alpha = \frac{1}{6} \sum_{i=1}^6 \text{mod} \left( \theta_i, \frac{\pi}{3} \right), \quad (5)$$

where  $\theta_i$  and  $\rho_i$  are the polar coordinates of  $\xi_i$ ,  $N$  is the size of the white input image and  $\text{mod}$  is the modulo function.

Finally, the lines along which the three cosines oscillate (color lines in Fig. 5), intersect at the offset phase  $\mathbf{o}$ . Considering only three peaks among the six not being symmetric, we define the oscillation lines as

$$L_{i=1,2,3}(\mathbf{x}) := x \sin \left( \theta_i + \frac{\pi}{2} \right) - y \cos \left( \theta_i + \frac{\pi}{2} \right) + \frac{F^P(\xi_i)}{2\pi} = 0, \quad (6)$$

where  $\mathbf{x} = (x, y)$ . We write the three line equations as  $A\mathbf{x} = B$  and its solution  $\mathbf{o} = (A^T A)^{-1} A^T B$  is estimated by least squares.

Note that our model is not a perfect fit of a real white image but in the Fourier domain it reproduces with high accuracy the behaviour of real white images. (Fig. 6)

For the comparison of our method with existing techniques, Fig. 7 show two crops of our result and the result of [12] using a white image captured with our Raytrix R5 in an integration sphere. The distance between the the calibrated centers is of the order of 0.1 pixels.

In the absence of ground-truth for plenoptic calibration, we have tested our algorithm with synthetic white plenoptic images, generated using Eq. 2. We have verified its robustness with many parameter values for  $\mathbf{o}$ ,  $\alpha$  and  $D$  simulating different plenoptic camera configurations. We have also added Gaussian noise of variance  $V$  and simulated different camera apertures by Gamma-correcting the white image by a factor  $\Gamma$ . For the sake of comparison, we have also estimated in all of our tested synthetic images the microlens images centers with the method of [12], a full spatial calibration method. Tab. I shows the average Euclidean distance between the real and estimated centers with the two methods. The error has been computed for different MLA configurations, amount of noise and the simulated apertures. In average, both methods are comparable but we have observed a larger robustness in our solution (smaller variance) when changing the parameters.

TABLE I: Errors (Euclidian distances) of our approach and the method in [12] with several parameter variations.

Parameters					Mean Error	
$D$	$\alpha$	$o_x, o_y$	$\Gamma$	$V_{(10^{-2})}$	Ours	[12]
10.1	0.03	-5 0	1.7	0.01	0.0821	<b>0.0365</b>
10.2	//	//	//	//	<b>0.1357</b>	0.3741
10.5	//	//	//	//	<b>0.3139</b>	0.3150
10.8	//	//	//	//	0.1886	<b>0.0209</b>
10	0.01	-5 0	1.7	0.01	0.0887	<b>0.0817</b>
//	0.04	//	//	//	0.0923	<b>0.0355</b>
//	0.05	//	//	//	<b>0.0929</b>	0.3288
//	0.1	//	//	//	0.0937	<b>0.0349</b>
10	0.03	-5.1 0	1.7	0.01	0.0911	<b>0.0280</b>
//	//	-5.5 0	//	//	<b>0.0982</b>	0.3165
//	//	-5 0.1	//	//	0.0905	<b>0.0379</b>
//	//	-5 0.5	//	//	<b>0.1168</b>	0.3489
10	0.03	-5 0	2	0.01	0.0882	<b>0.0590</b>
//	//	//	1.5	//	<b>0.0916</b>	0.3580
//	//	//	1	//	<b>0.0954</b>	0.4166
//	//	//	0.7	//	<b>0.0972</b>	Fail
10	0.03	-5 0	1.7	0.015	0.0900	<b>0.0410</b>
//	//	//	//	0.03	0.0893	<b>0.0776</b>
//	//	//	//	1	<b>0.0905</b>	0.3749
//	//	//	//	10	<b>0.0904</b>	Fail

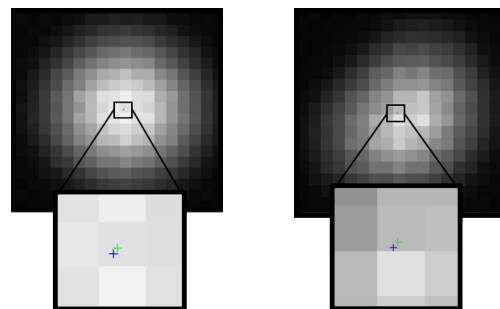


Fig. 7: Comparison of the calibration in [12] (green) and ours (blue) for two microlenses near the image center (left) and the image border (right), which has a cat-eye shape due to vignetting.

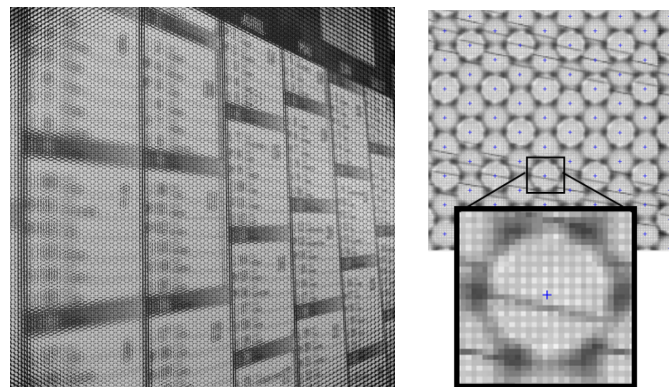


Fig. 8: Calibration on a natural raw plenoptic image (right) and a zoom on the microlenses calibration (left).

Also the algorithm in [12] has failed in two cases. While this error distances allow to measure the robustness of the proposed method, a calibration ground-truth would be required to assert the superiority of a calibration method over another.

Our model assumes  $D$  to be constant which is sound given that microlens manufacturing accuracy is of the order of 0.01 pixels (our calibration being accurate at  $\sim 0.1$  pixels). However, the sensor plane might be slightly tilted with respect to the MLA. We have not included this aspect in our implementation but it could be modeled knowing that such a tilt would make the 6 peaks to be around an ellipse. In that case the major and minor axis ratio would provide the angle tilt.

We have also noticed that the proposed method is extremely robust and does not require the images to be demosaicked. Also, we have observed that it would also work on natural images provided a bright uniform area appears in the scene (Fig. 8). In the case of video, it would be sufficient to integrate and clip the radiance of the raw image.

#### IV. PROPOSED DEPTH ESTIMATION METHOD

In this section we present our method for depth estimation. Unlike other methods we compute a *focus map* which gives the in-focus value of each pixel without using defocus cues but stereo matching. The novelty of our method is that we first compute a so-called *stereo focal stack*, then stereo matching is performed for each of the pairs of images of the stereo focal stack and, finally, the obtained disparities are combined to obtain a focus map.

##### A. Stereo Focal Stack Computation

A focal stack is a collection of photographs focused at different depths. In order to render each image (slice)  $I^g$  of the focal stack, refocused at the focal value  $g$ , we use the projection algorithm as in [13], [42]. This is, each pixel  $(x, y)$  of the raw LF  $R_{lf}$  belonging to the microlens with center coordinates  $(c_x, c_y)$ , is projected at position

$$(X, Y) = \left( s(g(x - c_x) + c_x), s(g(y - c_y) + c_y) \right), \quad (7)$$

where  $s$  controls the size of the rendered image. Formally, the refocused image is computed as

$$I^g(m, n) = \frac{1}{W(m, n)} \sum_{x, y} K(X - m, Y - n) R_{lf}(x, y),$$

$$\text{where } W(m, n) = \sum_{x, y} K(X - m, Y - n),$$

$$\text{and } K(u, v) = \begin{cases} \frac{1}{u^2 + v^2}, & \text{if } \|(u, v)\| < 0.5 \\ 0, & \text{otherwise.} \end{cases} \quad (8)$$

$K$  being a fixed kernel with a very small support (4 closest pixels from the projected coordinates).

Now, a *stereo focal stack* is rendered using Eq. 7 and Eq. 8 but separately for pixels  $(x, y)$  belonging to the left part and the right part of the microlens images (see Fig. 9). This strategy creates a stereo pair of images  $I_l^g$  and  $I_r^g$  for each focus value  $g$ .

The size  $s$  depends on the desired image size. A too large  $s$  leads to a low density in the refocusing plane of the projected points  $(X, Y)$ , requiring interpolation to fill the areas with no splatted pixels. In contrast, if  $s$  is too small, small details will be lost. Also, given a fixed size  $s$ , the spatial resolution on the

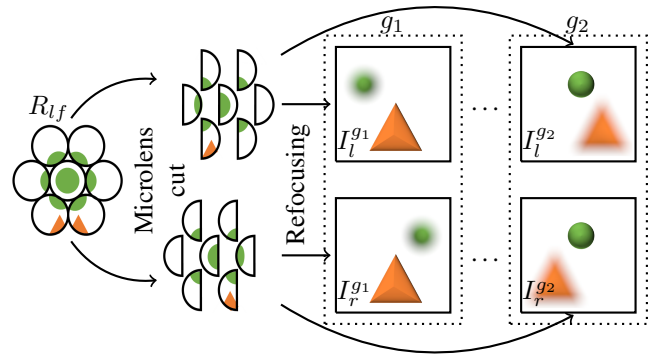


Fig. 9: Stereo focal stack computation. Points in the raw LF are projected separately depending on their positions on the microlens. Points belonging to the left (resp. right) side of the microlens are projected into  $I_l^g$  (resp.  $I_r^g$ ). For each  $g$ ,  $I_l^g$  and  $I_r^g$  is a rectified pair of stereo images such that points at the focus plane  $g$  appear sharp.

refocus plane depends on the depth of the scene as pointed out in [42].

In practice,  $s$  is chosen to be a good compromise for the range of depth values in the scene and the range of  $g$  is picked manually depending on the scene content. Besides, after fixing  $s$ , the projected points  $(X, Y)$  falling outside the refocus image plane are not considered, so all slices on the focal stack have the same size. Also inspired by [42], demosaicking is done during the rendering step, so the color channels separately are projected with Eq. 7.

##### B. Focus Map Estimation from the Stereo Focal Stack

In the following the pixels coordinates will be omitted but note that images, and focus and disparity maps are defined for each pixel  $(m, n)$ .

**Proposition 1.** *Let  $g_f$  be the value for which a certain point on the scene is in-focus. Then, for any focus value  $g$ , the difference between  $g$  and  $g_f$  is proportional to the disparity  $\Delta^g$  of this point in the stereo pair of images  $I_l^g$  and  $I_r^g$ . Also, a point appears in-focus in the refocused images  $I_l^g$  and  $I_r^g$  (i.e.  $g = g_f$ ) if and only if its corresponding disparity is null ( $\Delta^g = 0$ ).*

*Proof.* Let us consider a point in the scene that is seen by two microlenses (Fig. 10). The same reasoning is valid for more microlenses but we consider only two for the sake of clarity. Let  $x_1$  and  $x_2$  be the x-coordinates in  $R_{lf}$  of this point and  $\delta$  the distance between them. Using Eq. 7 we know that for each  $g$ , the disparity  $\Delta^g$  of the corresponding points in  $I_l^g$  and  $I_r^g$  is

$$\begin{aligned} \Delta^g &= X_2 - X_1 = s(g(x_2 - c_2) + c_2) - s(g(x_1 - c_1) + c_1) \\ &= s(g(\delta - D) + D). \end{aligned} \quad (9)$$

Now  $\Delta^g = 0$  if and only if

$$g = \frac{D}{D - \delta}, \quad (10)$$

which turns out to be the value  $g_f$  for which a point is in-focus (i.e. image points of a same scene point are projected at the same position).

From Eq. 9 and 10 we get the relationship between the refocusing parameter  $g$  used for rendering and  $g_f$  the value at which the point is in-focus

$$g = \frac{1}{s(\delta - D)} \Delta^g + g_f. \quad (11)$$

□

From the previous proposition we know that there is a linear relationship between  $g$  and  $\Delta^g$  and estimating the focus  $g_f$  is equivalent to estimating the value  $g$  such that  $\Delta^g = 0$ . In practice,  $g_f$  is estimated as the root of the line passing through two points  $(g_1, \Delta_1^g)$  and  $(g_2, \Delta_2^g)$  for two particular focus values  $g_1$  and  $g_2$ . Precisely,

$$g_f = \Delta_2^g - g_2 \frac{\Delta_1^g - \Delta_2^g}{g_1 - g_2}. \quad (12)$$

In order to compute Eq. 12, it is sufficient to render two pairs of stereo images at  $g_1$  and  $g_2$  and to estimate the corresponding disparities  $\Delta^{g_1}$  and  $\Delta^{g_2}$ . Notice, however, that it is possible to estimate the corresponding disparity  $\Delta^g$  for each slice of the focal stack. In that case  $g_f$  is the root of the regression line of all  $(g, \Delta^g)$ . This solution produces slightly more accurate results at the expense of greatly increasing the computational cost. This is why in our algorithm the focus map at each point is estimated using Eq. 12 which is a good trade-off between accuracy and complexity.

Note that, our algorithm does not compute SAIs but projects the information into the refocusing plane. Also, our focus map has the same size than the rendered images (same  $s$  value). Besides, it is interesting to point out that since the projection is done in a stereo focal stack it creates a parallax at each slice  $g$ . Thanks to this parallax, any binocular stereo algorithm can be exploited for evaluating  $\Delta^g$ . Depending on the desired accuracy and complexity any algorithm robust to blur can be used. In this work we have used the algorithm presented in [45] because it is multi-scale (thus robust to blur) real-time and accurate.

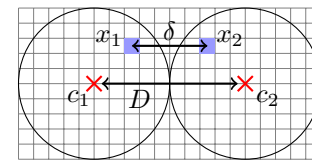
## V. RENDERING USING A FOCUS MAP

### A. Adaptive Splatting for Refocusing

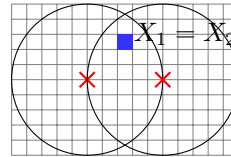
Inspired by [11], [13] we define a *splatting kernel*  $K'$  to be used instead of  $K$  in Eq. 8.  $K'$  adaptively changes for each point of the scene. In particular, we exploit the focus map obtained previously to define a Gaussian splatting kernel

$$K'(u, v) = \exp\left(-\frac{\sqrt{(X-u)^2 + (Y-v)^2}}{\lambda |g_f(u, v) - g| + \varepsilon}\right), \quad (13)$$

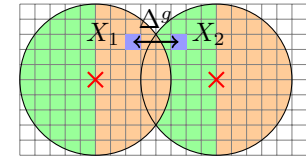
where  $\varepsilon$  is a very small value to avoid dividing by zero and  $\lambda$  controls the ratio among the spatial distance to  $(X, Y)$  and the  $g$  focus difference. The Gaussian kernel  $K'$  aims to penalize distant points from  $(X, Y)$  while its standard deviation results from the difference in absolute value between the refocusing value  $g$  and the in-focus value of the point  $g_f(u, v)$ .



(a) Raw LF



(b) Point in-focus in the refocused image ( $g = g_f$ )



(c) Point out-of-focus in the refocused image  $g \neq g_f$ . The left (green) and right (orange) parts of the microlenses form the left and right slices of the focal stack respectively.

Fig. 10: Projection of a scene point visible on two microlens images. Both points are projected at the same position ( $\Delta^g = 0$ ) when the point is in-focus ( $g = g_f$ ) and there is a shift  $\Delta^g \neq 0$  when the point is not in-focus.

The idea behind the weighting is that the kernel  $K'$  has a small support when the point is in-focus (i.e.  $g = g_f(u, v)$ ). On the contrary, the farther  $g$  is from  $g_f$ , the bigger the support of  $K'$  which increases blurriness at that particular point. Besides, the splatting strategy also helps to densify the rendered image. Indeed, we know that in particular cases several values of  $(x, y)$  are projected to the same point  $(X, Y)$  or different values of  $(X, Y)$  but very close from each other creating areas with few, or no pixel contributions [42].

One problem that rises, when using splatting is the spreading of background out-of-focus pixels intensities on foreground pixels, creating unwanted artifacts around edges of foreground objects. To overcome this issue we use a bilateral filtering strategy. We alter the kernel in such way that background pixel values are not propagated on the kernel area where the depth is inferior to the depth of the splatted pixel. The depth reshaped kernel is defined as  $K'' = K' \circ S$  where

$$S(u, v) = \begin{cases} 1, & \text{if } g_f([X], [Y]) > g_f(u, v), \\ 0, & \text{otherwise.} \end{cases} \quad (14)$$

Thus,  $S$  is not null when the point  $(u, v)$  is behind  $([X], [Y])$ . The refocusing is performed as in Eq. 8, replacing  $K$  with  $K''$ .

### B. Gathering for All-in-Focus Rendering

Splatting can also be seen backwards. Instead of spreading the ray values around the splatting coordinates, it is possible for a pixel  $(m, n)$  in the refocused image, knowing  $g_f$ , to compute the corresponding set of coordinates  $(x, y)$  of pixels in the raw LF that *see*  $(m, n)$ :

$$(x, y) = \left( \frac{\frac{u}{s} - c_x}{g_f(u, v)} + c_x, \quad \frac{\frac{v}{s} - c_y}{g_f(u, v)} + c_y \right). \quad (15)$$

We call this approach gathering, in the sense that we aim at integrating ray-pixels from the raw LF rather than projecting

them into a refocused image. Doing so, we integrate only the pixel describing the same scene point, creating an image that is sharp everywhere. This is similar to the approach proposed in [22], but in our case, the depth information is contained directly in the refocused image domain, not in the raw LF domain. Formally, the all in-focus image is computed as

$$I(m, n) = \frac{1}{W(m, n)} \sum_{c_x, c_y} K_{c_x, c_y}(m, n) R_{lf}([x], [y])$$

where  $W(m, n) = \sum_{c_x, c_y} K_{c_x, c_y}(m, n)$  and

$$K_{c_x, c_y}(m, n) = \begin{cases} \frac{1}{\{x\}^2 + \{y\}^2}, & \text{if } \|(x, y) - (c_x, c_y)\| < \frac{D}{2}, \\ 0, & \text{otherwise} \end{cases} \quad (16)$$

where  $\{a\}$  is the decimal part of  $a$  and  $K$  checks if the back-projected pixel is visible on a microlens image of center  $(c_x, c_y)$  (i.e. it is null if the back-projected pixel coordinates  $(x, y)$  is outside of the microlens image) and otherwise, weights the pixel contribution according to its distance from the (non-integer) back-projected image coordinates. Carrying the microlens image visibility test for all microlens images can be extremely heavy. However, a pixel  $(m, n)$  can only be seen within a small radius around  $(m/s, n/s)$  in the raw LF. That is why, in practice, the search for the microlens images can be bounded to few microlenses.

Note that depending on its depth, one pixel may receive incomplete color channel information. In that case, we interpolate with the neighbourhood pixels in the raw LF.

## VI. EXPERIMENTAL RESULTS

In this section we show the results of our depth estimation and rendering algorithms. We show experiments on Raytrix R5 data we have captured, on a Raytrix R11 dataset<sup>1</sup> and on the Georgiev’s dataset<sup>2</sup> for comparison purposes. As far as we know these are the only available type 2 plenoptic datasets providing raw data which is the input of our pipeline.

For the Raytrix datasets we use the calibration described in Sec. III on the white images we captured or the given white images from Raytrix. For the Georgiev dataset, the whites images not being available, we have manually calibrated them (squared big microlenses).

In our experiments we divide the raw LF by its corresponding white image to correct vignetting, and we fix  $s = 0.5$ . Our focus map is neither filtered nor regularized.

Fig. 11a shows the focus map of one of the images of the Raytrix R5 dataset. The two focus slices are rendered at  $g = 2.5$  and  $g = 5.5$ . The corresponding all-in-focus image in Fig. 11b is entirely sharp, demonstrating the validity of the focus map. Fig. 11c and Fig. 11d compare two images refocused using adaptive splatting, refocused on the background and the donkey flank respectively.

We notice that adapting the kernel allows to recover the details of the objects in-focus while showing a uniform blur in the out-of-focus areas.

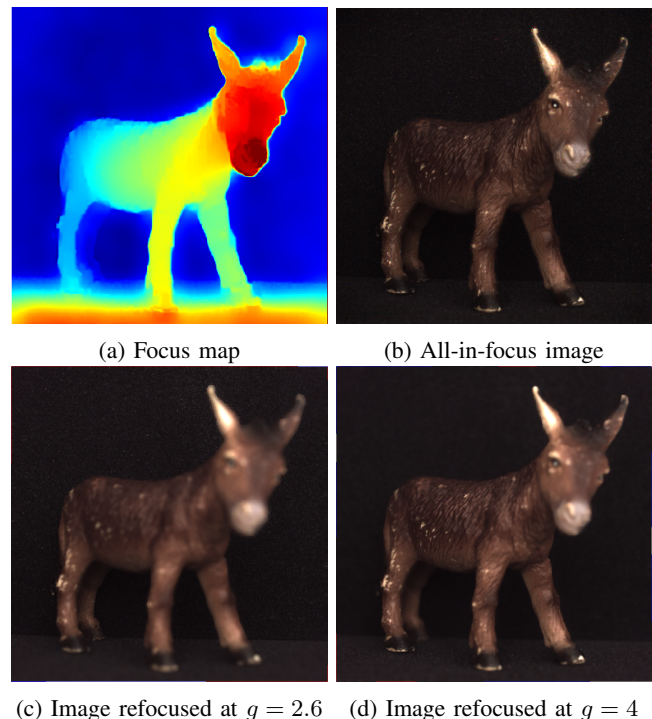


Fig. 11: *Donkey* experiment. Data captured with a Raytrix R5 camera. We invite the reader to zoom-in to see details. Supplementary material includes more results of our R5 dataset.

Supplementary material includes the raw data and calibration, as well as more examples of depth estimation and rendering of our R5 dataset.

Fig. 12 compares the obtained focus maps with the manufacturer depth map for a Raytrix R11 camera (most likely obtained with the microlens-based approach in [22]). We notice that the errors introduced by our method are essentially different than Raytrix’s.

Indeed our algorithm performs better in uniform areas (e.g. region between the arm and head of the pilot). However our algorithm is more sensitive to the reflexion halos (e.g. specularities into the ship’s wheel). Also, our algorithm generally has a better edge preservation while Raytrix depth maps suffer from *fattening* (e.g. branches of the forest). Fig.14 compares an all-in-focus image provided by Raytrix with ours. In general, our refocused images are comparable to Raytrix quality (more images can be found in the supplementary material).

On Fig. 13, we compare our depth maps with the results in [28], [40]. We can see that our method allows to recover more depth planes than the two microlens-bases approaches [28], [40]. This is due to the fact that our depth measurement is done on the image domain, with a bigger baseline than in the microlens domain. The depth maps for the rest of the Georgiev’s dataset are available in the supplementary material.

Regarding the refocusing, Fig. 15 shows how adaptive splatting compensates for angular aliasing and the sparse image sampling (pixels with no contribution are visible as 0 channel values) that arises when using a fixed splatting (Fig. 15a). The images on Fig. 15b to 15d show the effect of changing the blur parameter  $\lambda$ .

<sup>1</sup>Available online: <https://www.raytrix.de>  
<sup>2</sup>Available online: <http://www.tgeorgiev.net>



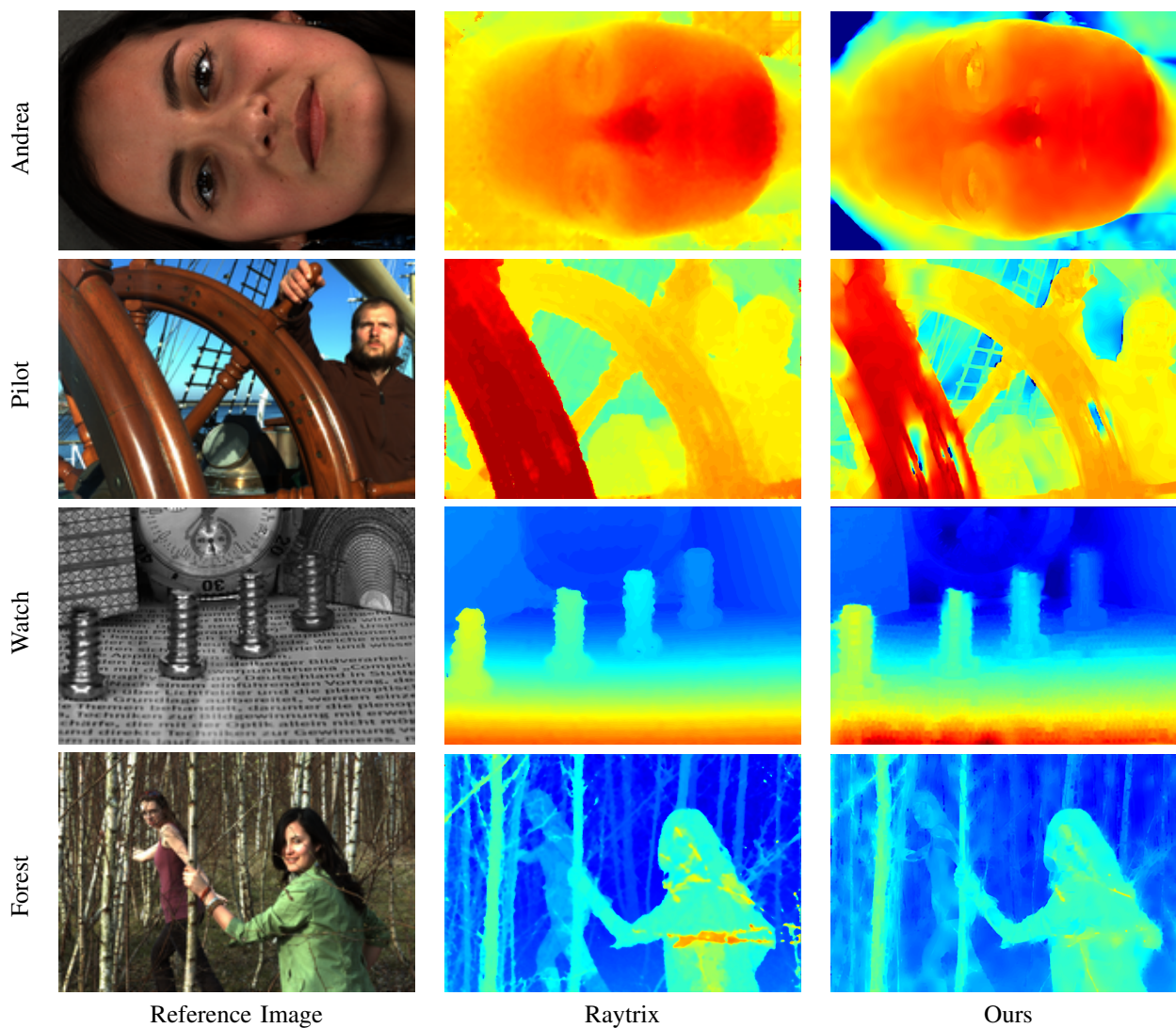


Fig. 12: Comparison of our depth maps with R11 test images provided by Raytrix. In general, our method deals better with objects borders and poor textured region but it provides erroneous disparities in specular regions.

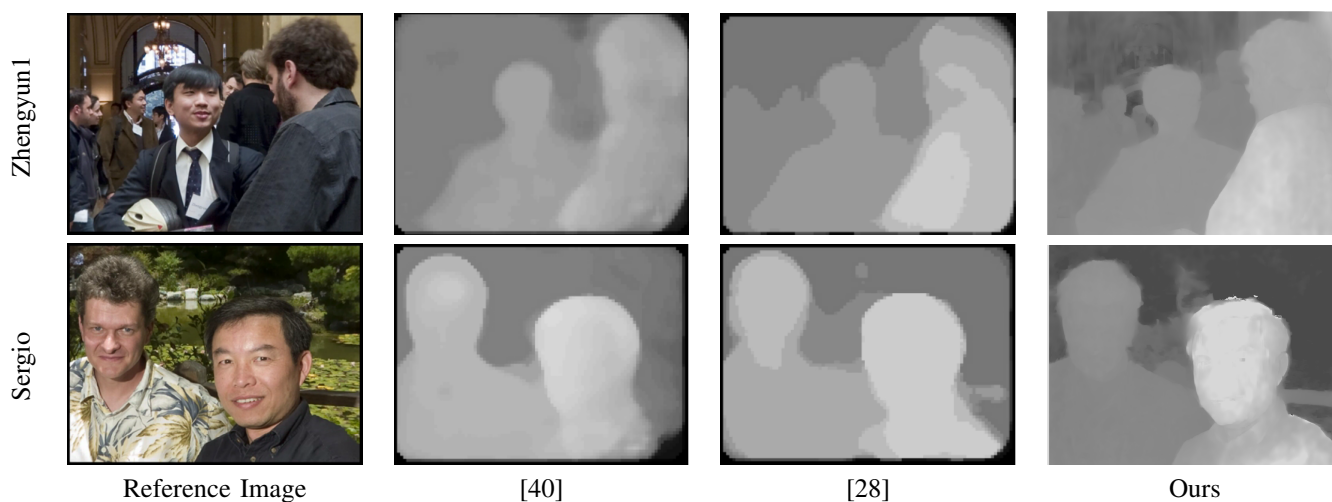


Fig. 13: Comparison of our depth maps with [40] and [28] using the Georgiev's dataset. Our approach is able to discern more depths and is more accurate. See the level of detail in the background of *Zhengyun1* or the faces in *Sergio*.

### Discussion :

Our microlens centers calibration algorithm has been tested with real white images and natural images captured with a Raytrix camera in addition to our simulated white images. We have observed that both estimations provide very close microlens image center positions for the great majority of the scenes we captured. Besides, our calibration method is fast (less than 0.2 seconds for Raytrix R5 images in our Matlab implementation) and could be used to monitor the microlens image center positions dynamically on a plenoptic video. These two features are of major interest if the plenoptic camera has a zoom lens or interchangeable lenses. In that situation, calibration could be done "on the fly" from the captured sequence which is not possible with existing methods.

Usually, the resolution of the final depth map is substantially smaller than the size of the raw LF for most of the state-of-the-art methods. In fact, the resolution depends on the considered image type for depth estimation (SAIs, microlens images, EPIs or refocused images). For instance, the size of each Lytro SAI is  $328 \times 328$  pixels which produces rather small depth maps (without super-resolution algorithms). In that sense, depth estimation on the refocused image plane provides the best resolution. In our approach, the resolution of the depth map and the rendered image are tuned with parameter  $s$ . The interesting point is that the depth map perfectly matches in terms of spatial resolution the rendered image which is a real advantage for depth-based editing tasks or in the rendering process itself as we have seen in Sec. V.

About the limitations of our approach, as for all the depth-based rendering approaches, errors during the depth estimation produce artifacts in the final images. When this occurs in uniform areas (which is often the case because of the stereo matching algorithm), it has few consequences on the rendering. However, for errors on textured zones, artifacts may be visible. Fortunately, stereo algorithms are usually robust in textured areas.

Also, even if the presented pipeline is particularly adapted for Raytrix cameras, we have not taken into account the trifocal property of the microlens array. Taking it in consideration during the splatting process will surely improve the rendering image quality.

Note that different disparity estimation algorithms could be used in our framework [46]. However, the goal of this paper is not to compare such methods but to show that the depth estimation problem in a plenoptic camera can be treated as a stereo problem via a stereo focal stack and without estimating SAIs. In fact, our depth estimation strategy could also be applied to type 1 data but it would not be optimal. In that case, our half-apertures would not capture all the angular information as all the SAIs do in a type 1. We believe however that this is a good alternative for focused plenoptic cameras for which SAIs are not available without errors.

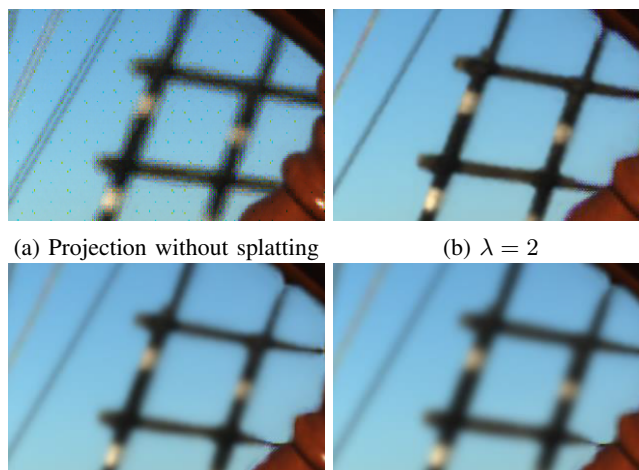
Moreover, it is interesting to point out that the proposed approach is somehow related to coded apertures [47]. Indeed, cutting the microlens images in half is equivalent to mask half of the aperture of a conventional camera. In particular, [48] compares the use of stereo aperture masks and depth from defocus using several masks and show that the second



(a) Raytrix

(b) Ours

Fig. 14: R11 all-in-focus rendering on test image Andrea. The fine details on the eyelashes are well recovered using our technique. Note that Raytrix uses a color and contrast correction and potentially a sharpening filter on their output images.



(a) Projection without splatting

(b)  $\lambda = 2$

(c)  $\lambda = 3$

(d)  $\lambda = 5$

Fig. 15: Refocusing via point projection without splatting using Eq. 8 (a) and adaptive splatting for different  $\lambda$  (b-d) on a region of the test image R11 Pilot. We can see that the adaptive strategy compensates for angular aliasing and that blur intensity can be controlled by the parameter  $\lambda$ .

provides a better depth discrimination. As the study focused on the setup where the focus depth is *fixed*, it would be interesting to see how this conclusion hold in our case, since the scene depth is *triangulated* using several artificial focus depths.

Finally, regarding the complexity, we believe our algorithm

is significantly lighter than other methods. Our Matlab implementation for generating the two slices of the focal stack runs in approximately 2.5 and 7 seconds per stereo slice for Raytrix R5 and R11 images respectively. We believe that a GPU implementation of our depth estimation and rendering can be done in real-time provided the used stereo algorithm is real-time.

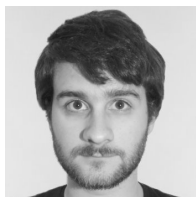
## VII. CONCLUSION

We have introduced a novel pipeline for processing focused plenoptic camera images. First we have presented a detailed description of our calibration algorithm that fully estimates all parameters in the Fourier domain allowing a fast and robust microlens images center estimation on white and natural images. Then, we have proposed a new algorithm for depth estimation from a stereo focal stack. Our algorithm does not require estimating SAIs or EPIs but can bring into play any stereo algorithm. Moreover, it provides a depth map in the refocused image domain, and does not require any knowledge about the camera parameters (except the microlens images centers, estimated at the beginning of our pipeline). Finally, our image rendering is guided by the estimated scene depth and allows to refocus the images or render all-in-focus images. We have tested our algorithm on images captured with a Raytrix camera but our modelling is not restricted to it and could be applied to other focused plenoptic cameras. Further work will include combining the defocus cues introduced by the stereo focal stack in order to improve the depth measurement, especially in the specular areas and occlusions.

## REFERENCES

- [1] R. Ng, "Digital light field photography," 2006.
- [2] T. G. Georgiev, A. Lumsdaine, and S. Goma, "High dynamic range image capture with plenoptic 2.0 camera," *Signal recovery and synthesis*, p. SWA7P, 2009.
- [3] F. P. Nava and J. Lücke, "Simultaneous estimation of super-resolved depth and all-in-focus images from a plenoptic camera," in *3DTV Conference: The True Vision-Capture, Transmission and Display of 3D Video*, 2009. IEEE, 2009, pp. 1–4.
- [4] "https://www.lytro.com."
- [5] A. Lumsdaine and T. Georgiev, "The focused plenoptic camera," in *Computational Photography (ICCP)*, 2009 *IEEE International Conference on*. IEEE, 2009, pp. 1–8.
- [6] "http://www.raytrix.de."
- [7] S. J. Gortler, R. Grzeszczuk, R. Szeliski, and M. F. Cohen, "The lumigraph," in *Proceedings of the 23rd annual conference on Computer graphics and interactive techniques*. ACM, 1996, pp. 43–54.
- [8] M. Levoy and P. Hanrahan, "Light field rendering," in *Proceedings of the 23rd annual conference on Computer graphics and interactive techniques*. ACM, 1996, pp. 31–42.
- [9] S. Wanner, J. Fehr, and B. Jaehne, "Generating epi representations of 4d light fields with a single lens focused plenoptic camera," in *International Symposium on Visual Computing (ISVC, oral presentation)*, 2011.
- [10] T. Georgiev and A. Lumsdaine, "Full resolution lightfield rendering," 2008.
- [11] C.-K. Liang and R. Ramamoorthi, "A light transport framework for lenslet light field cameras," *ACM Transactions on Graphics (TOG)*, vol. 34, no. 2, p. 16, 2015.
- [12] D. G. Dansereau, O. Pizarro, and S. B. Williams, "Decoding, calibration and rectification for lenselet-based plenoptic cameras," in *Computer Vision and Pattern Recognition (CVPR)*, 2013 *IEEE Conference on*. IEEE, 2013, pp. 1027–1034.
- [13] J. Fiss, B. Curless, and R. Szeliski, "Refocusing plenoptic images using depth-adaptive splatting," in *Computational Photography (ICCP)*, 2014 *IEEE International Conference on*. IEEE, 2014, pp. 1–9.
- [14] D. Cho, M. Lee, S. Kim, and Y.-W. Tai, "Modeling the calibration pipeline of the lytro camera for high quality light-field image reconstruction," in *Computer Vision (ICCV)*, 2013 *IEEE International Conference on*. IEEE, 2013, pp. 3280–3287.
- [15] E. H. Adelson and J. Y. A. Wang, "Single lens stereo with a plenoptic camera," *IEEE Transactions on Pattern Analysis & Machine Intelligence*, no. 2, pp. 99–106, 1992.
- [16] T. E. Bishop and P. Favaro, "Plenoptic depth estimation from multiple aliased views," in *Computer Vision Workshops (ICCV Workshops)*, 2009 *IEEE 12th International Conference on*. IEEE, 2009, pp. 1622–1629.
- [17] N. Sabater, M. Seifi, V. Drazic, G. Sandri, and P. Perez, "Accurate disparity estimation for plenoptic images," in *ECCV Workshop on Light Fields for Computer Vision*, 2014.
- [18] M.-J. Kim, T.-H. Oh, and I. S. Kweon, "Cost-aware depth map estimation for lytro camera," in *Image Processing (ICIP)*, 2014 *IEEE International Conference on*. IEEE, 2014, pp. 36–40.
- [19] S. Heber, R. Ranftl, and T. Pock, "Variational shape from light field," in *Energy Minimization Methods in Computer Vision and Pattern Recognition*. Springer Berlin Heidelberg, 2013, pp. 66–79.
- [20] H.-G. Jeon, J. Park, G. Choe, J. Park, Y. Bok, Y.-W. Tai, and I. S. Kweon, "Accurate depth map estimation from a lenslet light field camera," in *Proceedings of the IEEE Conference on Computer Vision and Pattern Recognition*, 2015, pp. 1547–1555.
- [21] T. Georgiev and A. Lumsdaine, "Focused plenoptic camera and rendering," *Journal of Electronic Imaging*, vol. 19, no. 2, pp. 021 106–021 106, 2010.
- [22] C. Perwass and L. Wietzke, "Single lens 3d-camera with extended depth-of-field," in *Proc. SPIE*, vol. 8291, 2012, p. 829108.
- [23] C.-W. Chang, M.-R. Chen, P.-H. Hsu, and Y.-C. Lu, "A pixel-based depth estimation algorithm and its hardware implementation for 4-d light field data," in *Circuits and Systems (ISCAS)*, 2014 *IEEE International Symposium on*. IEEE, 2014, pp. 786–789.
- [24] S. Tulyakov, T. H. Lee, and H. Han, "Quadratic formulation of disparity estimation problem for light-field camera," in *Image Processing (ICIP)*, 2013 *20th IEEE International Conference on*. IEEE, 2013, pp. 2063–2067.
- [25] O. Fleischmann and R. Koch, "Lens-based depth estimation for multi-focus plenoptic cameras," *Pattern Recognition*, pp. 410–420, 2014.
- [26] M. Uliyar, G. Putraya, S. Ukil, S. Basavaraja, K. Govindarao, and M. Veldandi, "Pixel resolution plenoptic disparity using cost aggregation," in *Image Processing (ICIP)*, 2014 *IEEE International Conference on*. IEEE, 2014, pp. 3847–3851.
- [27] S. Wanner, C. Straehle, and B. Goldluecke, "Globally consistent multi-label assignment on the ray space of 4d light fields," in *Computer Vision and Pattern Recognition (CVPR)*, 2013 *IEEE Conference on*. IEEE, 2013, pp. 1011–1018.
- [28] M. Uliyar, G. Putraya, and S. Basavaraja, "Fast epi based depth for plenoptic cameras," in *Image Processing (ICIP)*, 2013 *20th IEEE International Conference on*. IEEE, 2013, pp. 1–4.
- [29] M. W. Tao, S. Hadap, J. Malik, and R. Ramamoorthi, "Depth from combining defocus and correspondence using light-field cameras," in *Computer Vision (ICCV)*, 2013 *IEEE International Conference on*. IEEE, 2013, pp. 673–680.
- [30] M. W. Tao, P. P. Srinivasan, J. Malik, S. Rusinkiewicz, and R. Ramamoorthi, "Depth from shading, defocus, and correspondence using light-field angular coherence," in *Proceedings of the IEEE Conference on Computer Vision and Pattern Recognition*, 2015, pp. 1940–1948.
- [31] D. Dansereau and L. Bruton, "Gradient-based depth estimation from 4d light fields," in *Circuits and Systems, 2004. ISCAS'04. Proceedings of the 2004 International Symposium on*, vol. 3. IEEE, 2004, pp. III–549.
- [32] R. C. Bolles, H. H. Baker, and D. H. Marimont, "Epipolar-plane image analysis: An approach to determining structure from motion," *International Journal of Computer Vision*, vol. 1, no. 1, pp. 7–55, 1987.
- [33] Y.-H. Kao, C.-K. Liang, L.-W. Chang, and H. H. Chen, "Depth detection of light field," in *Acoustics, Speech and Signal Processing, 2007. ICASSP 2007. IEEE International Conference on*, vol. 1. IEEE, 2007, pp. I–893.
- [34] A. Mousnier, E. Vural, and C. Guillemot, "Partial light field tomographic reconstruction from a fixed-camera focal stack," *arXiv preprint arXiv:1503.01903*, 2015.
- [35] C. Chen, H. Lin, Z. Yu, S. Bing Kang, and J. Yu, "Light field stereo matching using bilateral statistics of surface cameras," in *Proceedings of the IEEE Conference on Computer Vision and Pattern Recognition*, 2014, pp. 1518–1525.

- [36] H. Lin, C. Chen, S. Bing Kang, and J. Yu, "Depth recovery from light field using focal stack symmetry," in *Proceedings of the IEEE International Conference on Computer Vision*, 2015, pp. 3451–3459.
- [37] W. Williem and I. Kyu Park, "Robust light field depth estimation for noisy scene with occlusion," in *Proceedings of the IEEE Conference on Computer Vision and Pattern Recognition*, 2016, pp. 4396–4404.
- [38] T.-C. Wang, A. A. Efros, and R. Ramamoorthi, "Occlusion-aware depth estimation using light-field cameras," in *Proceedings of the IEEE International Conference on Computer Vision*, 2015, pp. 3487–3495.
- [39] S. Heber and T. Pock, "Convolutional networks for shape from light field," in *Proceedings of the IEEE Conference on Computer Vision and Pattern Recognition*, 2016, pp. 3746–3754.
- [40] T. Georgiev and A. Lumsdaine, "Reducing plenoptic camera artifacts," in *Computer Graphics Forum*, vol. 29, no. 6. Wiley Online Library, 2010, pp. 1955–1968.
- [41] M. Seifi, N. Sabater, V. Drazic, and P. Perez, "Disparity guided demosaicking of light field images," in *IEEE International Conference on Image Processing (ICIP)*, 2014.
- [42] Z. Yu, J. Yu, A. Lumsdaine, and T. Georgiev, "An analysis of color demosaicing in plenoptic cameras," in *Computer Vision and Pattern Recognition (CVPR), 2012 IEEE Conference on*. IEEE, 2012, pp. 901–908.
- [43] Y. Bok, H.-G. Jeon, and I. S. Kweon, "Geometric calibration of micro-lens-based light-field cameras using line features," in *Proceedings of European Conference on Computer Vision (ECCV)*, 2014.
- [44] B. G. Quinn, "Estimating frequency by interpolation using fourier coefficients," *Signal Processing, IEEE Transactions on*, vol. 42, no. 5, pp. 1264–1268, 1994.
- [45] V. Drazic and N. Sabater, "A precise real-time stereo algorithm," in *Proceedings of the 27th Conference on Image and Vision Computing New Zealand*. ACM, 2012, pp. 138–143.
- [46] D. Scharstein and R. Szeliski, "A taxonomy and evaluation of dense two-frame stereo correspondence algorithms," *International journal of computer vision*, vol. 47, no. 1-3, pp. 7–42, 2002.
- [47] A. Levin, R. Fergus, F. Durand, and W. Freeman, "Image and depth from a conventional camera with a coded aperture," in *TOG*, vol. 26, no. 3, 2007, p. 70.
- [48] A. Levin, "Analyzing depth from coded aperture sets," in *ECCV*. Springer, 2010, pp. 214–227.



**Matthieu Hog** received the BSc in 2013 from the Université de Saint-Etienne, France and the MSc in 2015 from the Université de Saint-Etienne and the Gjøvik University College, Norway. He is currently pursuing his PhD studies in INRIA (Institut National de Recherche en Informatique et en Automatique) and Technicolor Research & Innovation in Rennes, France. His research interests are image processing, computer vision and computational imaging.



**Neus Sabater** received the BSc degree in 2005 from the Universitat de Barcelona, Spain, and the MSc and PhD degrees in 2006 and 2009, respectively, in image processing from the Ecole Normale Supérieure de Cachan, France. She was a postdoctoral researcher at the California Institute of Technology before being appointed at Technicolor Research & Innovation in 2011 where she is currently a Senior Scientist. Her research interest include image processing, computer vision and computational photography.



tography.

**Benoît Vandame** received the MSc degree in 1997 from the Université de Saint-Etienne, France, and the PhD degrees in 2004 from the Université de Nice, dedicated to image processing applied to large datasets of astronomical images. He was a postdoctoral researcher at the European Southern Observatory (ESO München, Germany) before being appointed at the Canon Research Center in Rennes, France. In 2014 he joins the Technicolor Research & Innovation. His research interest include image processing, computer vision and computational pho-



**Valter Drazic** received the MSc degree in Optical Engineering from Telecom Physique, Strasbourg in 1988, a MSc degree in Physics from Université Louis Pasteur, Strasbourg in 1989 and a PhD degree from Karlsruhe Institute of Technology in 1993. He is currently Principal Scientist with Technicolor Research & Innovation. His main research activities spanned from illumination and imaging optics, displays, computer vision, acquisition technologies and computational imaging.